On the thermal impact of gas venting and hydrate crystallization

Duo Fu Chen

Key Laboratory of Marginal Sea Geology of Guangzhou Institute of Geochemistry, Chinese Academy of Sciences, Wushan, China

Gas Hydrate Research Center, Chinese Academy of Sciences, Wushan, China

Lawrence M. Cathles

Department of Earth and Atmospheric Sciences, Cornell University, Ithaca, New York, USA

Received 10 November 2004; revised 6 May 2005; accepted 9 June 2005; published 10 November 2005.

[1] At the gas venting rates observed in some seafloor localities, heat advection and the latent heat of hydrate crystallization could significantly warm the subsurface, reduce the hydrate stability zone thickness, and decompose previously crystallized hydrate. Effects of heat advection and the latent heat of hydrate crystallization are limited by the duration of time over which venting occurs and ultimately by the time it takes to plug vents with hydrate, however. We examine the connection between gas venting, hydrate crystallization, and subsurface temperature using a new one-dimensional analytical solution to the steady state heat flow equation with constant hydrate crystallization, and we examine the effects of the duration of venting employing one-dimensional finite element solutions to the transient heat flow equation that include space- and time-dependent hydrate dissolution and crystallization. We show that if lateral losses of heat are negligible, hydrate crystallization and the advection of heat by gas flow at the more vigorous rates of gas discharge observed on the seafloor could increase the temperature gradient near the surface by more than an order of magnitude and decrease the feed gas hydrate stability zone thickness from ~570 to <200 m before the vents plug with hydrate. We compute how the chemistry of the venting gas and crystallizing hydrate evolve as a vent plugs with hydrate.

Citation: Chen, D. F., and L. M. Cathles (2005), On the thermal impact of gas venting and hydrate crystallization, *J. Geophys. Res.*, *110*, B11204, doi:10.1029/2004JB003533.

1. Introduction

[2] Gas hydrate is an ice-like crystalline mineral in which hydrocarbon and nonhydrocarbon gases are enclosed in a rigid cage of water molecules [*Sloan*, 1998]. It is believed the world's shelves, continental slopes, and arctic permafrost host a hydrate gas resource equal in size to that of all the fossil fuels combined (~10^{19} g carbon [*Kvenvolden and Lorenson*, 2001]). Because of the size of this resource, the instability of hydrate accumulations, and the potential for hydrate decomposition to add methane to the atmosphere and contribute to global warming, hydrates are today an active area of hydrocarbon research.

[3] Two end-member types of hydrate accumulation have been identified on the seafloor and modeled. The first type is associated with bottom simulating seismic reflections (BSRs) and occurs in areas of low sedimentation where gas leakage is dispersed, widespread, and slow. The BSR on the seismic profile lies between a hydrate layer which contains very little pore space gas from an underlying layer which contains appreciable trapped pore space gas [e.g., *Dickens and Quinby-Hunt*, 1997; *Rempel and Buffett*, 1997; *Hyndman and Davis*, 1992; *Xu and Ruppel*, 1999]. Hydrate accumulation is controlled by heat and mass balance. Hydrate accumulates over long periods of time and the top of hydrate lies below the seafloor at a depth at which methane diffusion to the ocean is slow [e.g., *Rempel and Buffett*, 1997; *Xu and Ruppel*, 1999]. Gas does not move through the hydrate layer as a separate phase. The other end-member type of seafloor hydrate accumulation occurs at gas vents. The Bush Hill hydrate mound in Green Canyon Block 184 off the Louisiana coast is perhaps the best known example. There, gas passes through the entire hydrate stability zone and bubbles into the overlying ocean. The rate of hydrate crystallization from the gas streams depends on the kinetics of hydrate crystallization as well as heat and mass balance. This paper considers the thermal effects of gas venting and hydrate crystallization in this second type of hydrate accumulation by adding heat advection and the latent heat of hydrate crystallization to compositional kinetic models of hydrate crystallization that have previously developed by *Chen and Cathles* [2003], *Cathles and Chen* [2004] and *Chen et al.* [2004].

[4] The potential impact of heat advection by gas flow and the latent of hydrate crystallization can be illustrated by reference to gas venting rates that have been measured on the Bush Hill hydrate mound (Figure 1). Bubble streams are

Copyright 2005 by the American Geophysical Union.
0148-0227/05/2004JB003533$09.00

localized in a 100 m wide by 250 m long area of the 500 m dismeter Bush Hill mound where a N-S antithetic fault cuts across the mound [*MacDonald et al.*, 2003; *De Beukelaer et al.*, 2003]. *Leifer and MacDonald* [2003] measured a pulsing venting rate at one of the bubble streams at 26 tons of methane per year. A steady bubble stream a few meters away discharged at 3.8 t yr^{-1}. They indicate that about 10 bubble streams might exist the 250 × 100 m area. If all the vents were as strong as the one measured, the total venting rate would be 300 t yr^{-1}, and the average gas flux over the 100 × 250 m area would be 12 kg m^{-2} yr^{-1}, as illustrated in Figure 1.

[5] The Peclet number, *Pe*, for a one-dimensional vertical flow of gas from 1 km depth at 12 kg m^{-2} yr^{-1} is 1.13 (e.g., $Pe = q_g c_g z_b/K = 1.13$, where the thermal conductivity of the sediment K = 1 W m^{-1} °C^{-1}, the heat capacity of the gas c_g = 3000 J kg^{-1} °C^{-1}, the depth extent of the flow z_b = 1000 m, and the gas mass flux q_g = 12 kg m^{-2} yr^{-1}). Vertical flow with a Peclet number of 1.13 will increase the surface temperature gradient by a factor of 1.7($= Pe/1 - e^{-Pe}$ [see *Bredehoeft and Popadopulos*, 1965]). A gas flux of 12 kg (m^2 yr)$^{-1}$ could thus increase the surface thermal gradient from 20 to 33°C/km. If 10 wt% of the gas stream crystallizes as hydrate, which *Chen and Cathles* [2003] found was on average the case for the Bush Hill venting, and the latent heat of hydrate crystallization L = 421 J g^{-1}, gas entering the base of the hydrate stability zone (HSZ) at 12 kg (m^2 yr)$^{-1}$ will release heat at a rate of ~16 mW m^{-2}, which would raise the heat flow from ~30 [*Cathles and Losh*, 2004, and references cited therein] to 46 mW m^{-2}, and could increase the surface temperature gradient from 33 to ~43°C km^{-1}. If there were no conductive or advective heat losses, filling the pores of a sediment with 30% porosity with hydrate of density 800 kg m^{-3} would increase the local temperature by ~34°C, assuming the water saturated sediment heat capacity is 2934 kJ m^{-3} °C^{-1}. Bush Hill is a fairly weak gas vent with a small area of hydrate accumulation [*Milkov and Sassen*, 2003]. The venting rates at the larger areas seem also to be larger [*De Beukelaer et al.*, 2003].

[6] These simple calculations show that gas venting at rates similar to those observed on the seafloor at Bush Hill could affect subsurface temperatures in a way that would be both easily measurable and potentially significant for the hydrate resource that could accumulate (e.g., doubling the temperature gradient would halve the thickness of the HSZ and halve the hydrate resource in an area). The situation is complicated by several factors, however. Conductive heat losses are significant if the gas vents are narrow, although the conductive losses could be offset to some degree if water advects heat as well as gas. The dissolution of early crystallized hydrate will consume heat and retard heating. Crystallization of gas hydrate could plug the pores causing

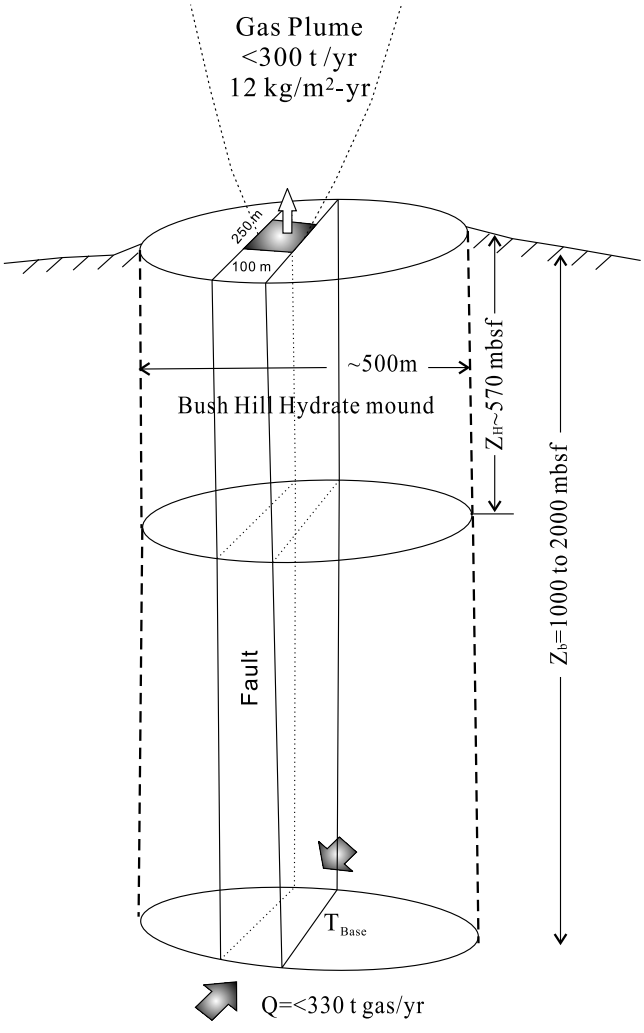

Figure 1. Sketch of gas venting, as it is currently understood, at the ~500 m diameter Bush Hill hydrate mound in Green Canyon Block 185, offshore Louisiana, Gulf of Mexico. The hydrate accumulated over the last ~10,000 years over an antithetic fault spur of the fault system which contains Connoco's Jolliet reservoirs at ~1.2–2.4 km depth [*Cook and D'Onfro*, 1991; *Roberts and Carney*, 1997]. The vent gas chemistry indicates that on average ~9% of the venting gas crystallizes as hydrate in the subsurface, and modeling suggests that hydrate will crystallize fairly uniformly to the base of the hydrate stability zone at ~570 m depth [*Chen and Cathles*, 2003]. The most recent venting appears to be localized in a ~250 m long interval of a 100 m wide N-S band where the antithetic fault currently cuts across the mound, and up to 10 bubble streams may exist in this area [*De Beukelaer et al.*, 2003]. Two bubble streams a few meters apart near the center of the mound are venting methane at a combined rate of ~30 t yr^{-1} [*Leifer and MacDonald*, 2003]. If the other bubble streams are of similar magnitude, methane gas might be entering the mound at ~330 t yr^{-1}, crystallizing ~30 t yr^{-1} of hydrate within the mound, and discharging ~300 t yr^{-1} of methane into the ocean. For the calculations presented here we assume that gas moves into the fault by horizontal flow at z_b and that the temperature at this depth is constant and equal to that which is normal (ambient) for the area. This figure provides a context for our calculations but would not meet the criteria for valid one-dimensional flow temperature simulations because the vertical interval of venting, z_b, is greater than the dimensions of the area from which gas is venting.

venting to shift to another location before major advective subsurface temperature changes could be realized.

[7] The purpose of this paper is to theoretically investigate the effect of gas venting and hydrate crystallization on subsurface temperature and hydrate stability. We concentrate in this paper on one-dimensional simulations, effectively assuming lateral heat losses are negligible. One-dimensional models will not adequately characterize the thermal effects of gas venting if the diameter of vertical gas venting is less than the depth at which the vertical gas flow originates. This criterion restricts application of the models presented here to areas where gas venting occurs fairly uniformly over areas of $\sim$1 km^2. A companion paper will consider lateral heat transfer from narrow, axially symmetric vents. Here we first derive a steady state analytical solution of the heat balance equation that shows how much the subsurface temperature profile could be altered by gas advection and latent heat released by hydrate crystallization. We then present transient finite element simulations of the evolution of hydrate crystallization and composition as a local gas vent channel warms and plugs with hydrate.

2. Theory

2.1. Model Framework

[8] Seismic wipe out zones and areas of hazy seismic reflection have proved a useful, if equivocal, way to map the presence of gas and hydrate in sediments [*Milkov and Sassen*, 2003; *MacDonald et al.*, 2003]. Gas vents are frequently located along fault zones, and gas appears in many cases to be drawn to sites of venting along the fault from a much more extensive band of gas saturation along the fault. Gas wipe out zones along the antithetic fault that cuts across the Bush Hill mound, for example, suggest that gas is drawn to the vents there from several kilometers to the north and south [*MacDonald et al.*, 2003]. In some cases the horizontal flow might be localized in a sand layer. If the gas upwelling in a portion of a fault zone is fed by horizontal gas flow, the temperature where this gas flow enters the fault zone will tend to maintained at normal ambient (see Figure 1). Assuming that significant horizontal flow enters the fault zone at some depth, we adopt a boundary condition in our 1-D modeling in which the temperature at that depth is constant at its ambient value. For example, in our calculations we assume an ambient temperature gradient of $\sim$20°C km^{-1} and an average seafloor temperature of $\sim$7°C. The base temperature boundary condition we use in modeling is thus either 27°C or 47°C, depending on whether our model gas source lies 1 km or 2 km below the seafloor.

2.2. Steady State Analytical Equilibrium Model

[9] Insight is provided by an analytical solution of the temperature equation with gas advection and latent heat release by gas crystallization. Under steady state conditions the heat transport at any depth must be constant. If the vertical axis is positive upward, this condition can be expressed as

$$-K\frac{\partial T}{\partial z} + q_b^g\left(c_g + R_{wg}c_w\right) = j_b + S(z - z_H), \tag{1}$$

where the first term describes heat conduction and the second advection by gas and water flow, j_b is the heat flux into the base of the system, and S is the latent heat released by hydrate crystallization from the base of the hydrate layer, z_H, to the surface. The parameters are defined in Table 1. The gas flux, q_b^g, is assumed here to be constant (even though at Bush Hill, on average, it decreases by $\sim$10% across the hydrate layer). The possibility that water as well as gas may be advected vertically is accommodated by the parameter, R_{wg}, the ratio of water to gas mass flux. The heat source term, S, is related to hydrate crystallization:

$$S = \frac{0.1q_b^g L}{|z_H|}, \tag{2}$$

where L is the latent heat of hydrate crystallization. We assume that hydrate crystallization occurs uniformly from the base of the hydrate stability zone, z_H, to the surface, and that 10% of the gas stream crystallizes as hydrate over this interval (hence the factor of 0.1 in (2)).

[10] Equation (1) is a first-order, linear differential equations that can be solved by standard methods [e.g., *Hochstadt*, 1964, p. 37]. The solution for constant z_H is

$$T = \frac{1}{a_1}\left[j_b\left(1 - e^{-a_1/a_o z}\right) - Sz_H\left(1 - e^{-a_1/a_o z'}\right) + Sz' - \frac{Sa_o}{a_1} \cdot \left(1 - e^{-a_1/a_o z'}\right)\right] \tag{3a}$$

$$j_b = \left[a_1 T_b + Sz_H\left(1 - e^{-a_1/a_o z_H}\right) - Sz_H - \frac{Sa_o}{a_1}\left(1 - e^{-a_1/a_o z_H}\right)\right] \Big/ \left(1 - e^{-a_1/a_o z_b}\right) \tag{3b}$$

$$\begin{aligned} a_1 &= -K \\ a_o &= q_b^g\left(c_g + R_{wg}c_w\right) \\ z' &= z, \qquad z > z_H \\ z' &= z_H, \qquad z \le z_H \end{aligned} \tag{3c}$$

where the subscript b indicates that the variable value applies at the base of the model system. In the limit of small a_o, (3a) becomes the normal radiogenic heat flow equation [*Turcotte and Schubert*, 2002, equation 4–17]. Substitution of equation (3b) into (3a) applies a constant temperature rather than a constant heat flow boundary condition at the base of the system. When $S = 0$ this equation reduces to the well known advective temperature profile of *Bredehoeft and Popadopulos* [1965].

2.3. Transient Finite Element Model

[11] We use finite element methods to solve the transient temperature equation

$$\rho_m c_m \frac{DT}{Dt} = \frac{\partial}{\partial z}K\frac{\partial T}{\partial z} - \left(c_g + R_{wg}c_w\right)q^g\frac{\partial T}{\partial z} + S. \tag{4}$$

Parameters are defined in Table 1. Notice that the gas mass flux, q^g, can now vary with depth and time. There is no superscript "b" as there was in the analytical equations

Table 1. Glossary of Parameters With Values Used in Modeling in This Paper and References

Symbol	Definition	Value	Reference
$\overline{T}_e$	average temperature in element e [°C]		
$\overline{P}_e$	average hydrostatic pressure in element e [Pa]		
z	depth [m], negative down from seafloor		
q_b^g	mass flux gas [kg m^{-2} yr^{-1}] at base of model		
$q_{b,\min}^g$	reference minimal gas mass flux [kg m^{-2} yr^{-1}] at base of model	1.8	*Chen and Cathles* [2003] and *Cathles and Chen* [2004]
q^g	mass flux of gas above base of system		
c_g	heat capacity of gas [J kg^{-1} °C^{-1}]	3000	
c_w	heat capacity of water [J kg^{-1} °C^{-1}]	4186	
$\rho_m c_m$	heat capacity of sediment [J m^{-3} °C^{-1}]	2958	
K	thermal conductivity [W m^{-1} °C^{-1}]	~1	*Revil and Cathles* [2002]
R_{wg}	ratio of mass flux of water to gas		
L	latent heat of hydrate crystallization [J kg^{-1}]	416,000	*Rueff et al.* [1988]
S	heat generation by hydrate crystallization or dissolution [J m^{-3} s^{-1}]		
k	kinetic rate constant [kg m^{-2} yr^{-1}]	3.5×10^{-4}	*Cathles and Chen* [2004]
k_{mul}	multiplier of rate constant and divisor of time steps	$= q_b^g$	
k_{adj}	multiplier of kinetic rate constant used to make the average fractional crystallization of gas ~0.1		
t_{adj}	multiplier of time steps used to allow hydrate crystallized over simulation to fill the pore space		
S_k	ratio of dissolution to crystallization kinetics	1	
l_e	length of element [m]		
E/R	activation energy/gas constant [°C]	10,000	*Chen and Cathles* [2003]
α_i	T-dependent coefficients in equation (6)		*Chen and Cathles* [2003]
F_e^{cryst}	fraction of gas mass entering element e over Δt that is crystallized as hydrate		
${}^{\text{kinetic}}F_{je}^{\text{cryst}}$	fractional increase of gas mass entering element e over Δt due to dissolution of bin j hydrate		
${}^{\text{available}}F_{je}^{\text{cryst}}$	maximum fractional increase in gas mass entering element e over Δt that can be produced by total dissolution of bin j hydrate		
${}^{\text{thermodyn}}F_{je}^{\text{cryst}}$	maximum fractional increase in gas mass entering element e over Δt that can be produced by total dissolution of bin j hydrate before gas is saturated with respect to bin j hydrate		
F_{je}^{dissol}	$= \min [{}^{\text{kinetic}}F_{je}^{\text{cryst}}, {}^{\text{available}}F_{je}^{\text{cryst}}, {}^{\text{thermodyn}}F_{je}^{\text{cryst}}]$, the actual fractional increase in gas mass flux due to dissolution of bin j hydrate in element e		
F_e	fraction of gas flux into element e due to both crystallization and dissolution		
F	fractional loss or gain of feed gas across system		
X_e^g	mass fraction $C_3 + C_4$ in gas in element e		
X_f^{g-eq}	fictive (subscript f) mass fraction of $C_3 + C_4$ at which crystallization of hydrate will cease		*Chen and Cathles* [2003]
X_{je}^{g-eqH}	mass fraction of C_3+C_4 of gas that is in equilibrium in element e with hydrate of bin j composition		
X_{je}^{Hyd}	average mass fraction of $C_3 + C_4$ in gas enclathrated in hydrate of bin j composition in element e		
ϕ	sediment porosity		
ϕ_o	uncompacted sediment porosity	0.43	
$\phi_{\min}$	minimum sediment porosity	0.1	
S_H	fraction of pore space filled with hydrate		
β	sediment compressibility [Pa^{-1}]	1.41×10^{-8}	*Revil and Cathles* [2002]
ρ_G	density of sediment grains [kg m^{-3}]	2700	
ρ_w	density of water [kg m^{-3}]	1000	

above. Gas is still introduced at the base of the model system at a rate q_b^g, but above the base the rate changes due to hydrate dissolution and crystallization. Thermal conductivity, K, is defined in our model as a function of porosity and temperature using the fabric theory approach [*Luo et al.*, 1994], assuming hydrate has the same thermal properties as water (see Table 1). Sediments with shale composition are compacted using parameters in Table 1 as described by *Revil and Cathles* [2002] assuming pore pressure is hydrostatic.

[12] The heat source term, S, and the gas mass flux, q^g, are determined by a propagator kinetic model described by *Cathles and Chen* [2004]. As described there, the fractional decrease in gas mass flux due to hydrate crystallization in an element e is determined by a first-order rate equation

$$F_e^{cryst} = \frac{-kl_e \Delta X_e^g}{q_e^g} \exp\left(\frac{E}{R}\left(\frac{1}{T^*} - \frac{1}{\overline{T}_e}\right)\right), \tag{5}$$

$$\begin{aligned} \Delta X_e^g &= X_e^g - X_f^{g-eq}, & X_e^g &> X_f^{g-eq} \\ \Delta X_e^g &= 0, & X_e^g &\le X_f^{g-eq} \end{aligned}$$

where k [kg (m^3 yr) $^{-1}$] is the rate constant, X_e^g is the (average) mass fraction $C_3 + C_4$ of gas in element e, and X_j^{g-eq} is the fictive (subscript f) mass fraction $C_3 + C_4$ in the gas of element e at which the rate of hydrate crystallization would be zero. X_j^{g-eq} can be described as polynomial function of the average temperature and pressure in the element [*Chen and Cathles*, 2003], e.g., $X_j^{g-eq} = X_j^{g-eq}(\overline{P}_e, \overline{T}_e)$. The composition of hydrate crystallized in element e can be described by a power series in X_e^g with temperature-dependent coefficients [*Chen and Cathles*, 2003]:

$$X_e^{\mathrm{Hyd}} = \alpha_o(\overline{T}_e) + \alpha_i(\overline{T}_e)\left(X_e^{g-eqH}\right)^i. \tag{6}$$

Here α_ι are linear functions of temperature, i ranges from 1 to 3, and summation is assumed over the repeated i indices. The hydrate crystallized in the element is added to one of the 22 numerical hydrate bins within which X_e^{Hyd} falls (see Table 2). Note that this model assumes the rate of hydrate crystallization is linearly proportional to the degree of chemical disequilibrium with hydrate as measured by the $C_3 + C_4$ mass fraction in the gas. We assume pore waters have seawater salinity in our thermodynamic calculations. Full details are given by *Chen and Cathles* [2003].

[13] Hydrate that has crystallized in an element may dissolve if the gas in the element has a mass fraction $C_3 + C_4$ less than that which would be in equilibrium with any hydrate in the element (e.g., $X_e^g < X_j^{g-eq}$, where X_j^{g-eq} is the mass fraction of $C_3 + C_4$ in the gas stream that would be is in equilibrium with hydrate in bin j with composition X_{je}^{Hyd}). If the dissolution is kinetically controlled, the fractional increase in the gas mass flux entering an element due to hydrate dissolution can be described [*Cathles and Chen*, 2004] as

$${}^{\mathrm{kinetic}}F_{je}^{\mathrm{dissol}} = \frac{-kS_k l_e \Delta X_{je}^g}{q_e^g} \exp\left[\frac{E}{R}\left(\frac{1}{T^*} - \frac{1}{\overline{T}_e}\right)\right] \tag{7a}$$

$$\Delta X_{je}^g = X_e^g - X_j^{g-eqH}\left(X_{je}^{Hyd}, \overline{T}_e\right), \quad X_e^g < X_j^{g-eqH}$$

$$\Delta X_e^g = 0, \qquad X_e^g \geq X_j^{g-eqH}$$

Here the gas added to the gas stream through element e derives from the dissolution of hydrate with the composition range of hydrate bin "j" within the element e (see Table 2). The kinetic rate constant k is the same as in (5) but a dimensionless parameter S_k has been added that allows the dissolution kinetics to be increased or decreased with respect to the crystallization kinetics. The equilibrium relation between hydrate and gas is defined by equation (6).

[14] The increase (across an element) in gas mass flux of bin j composition due to the dissolution of hydrate from bin j over a time step Δt cannot exceed the mass of gas stored in the hydrate in that bin. This availability maximum can be expressed as

$${}^{\mathrm{available}}F_{je}^{\mathrm{dissol}} \leq \frac{G_j l_e}{q_e^g \Delta t}, \tag{7b}$$

where G_j is the mass of gas in hydrate compositional bin j per m^3 of sediment.

Table 2. Average Composition (Mass Fraction $C_3 + C_4$) of Hydrate in the Computational Bins

	Bin Boundary			
Bin Numbers j	Bottom	Top	Bin Width	$\overline{X}_j^{\mathrm{Hyd}}$
1	0.000	0.032	0.032	0.016
2	0.032	0.062	0.030	0.047
3	0.062	0.091	0.029	0.077
4	0.091	0.118	0.027	0.105
5	0.118	0.144	0.026	0.131
6	0.144	0.169	0.025	0.157
7	0.169	0.192	0.023	0.181
8	0.192	0.214	0.022	0.203
9	0.214	0.235	0.021	0.225
10	0.235	0.256	0.021	0.246
11	0.256	0.275	0.019	0.266
12	0.275	0.293	0.018	0.284
13	0.293	0.310	0.017	0.302
14	0.310	0.326	0.016	0.318
15	0.326	0.342	0.016	0.334
16	0.342	0.357	0.015	0.350
17	0.357	0.371	0.014	0.364
18	0.371	0.384	0.013	0.378
19	0.384	0.397	0.013	0.391
20	0.397	0.409	0.012	0.403
21	0.409	0.420	0.011	0.415
22	0.420	∞	∞	>0.420

[15] If the kinetics are very fast (e.g., S_k larger than $\sim$100) and there is enough hydrate in bin j that it is not dissolved in Δt, the gas will saturate with respect to bin j hydrate, and the fractional increase in the gas mass flux will be

$${}^{\mathrm{thermodyn}}F_{je}^{\mathrm{cryst}} = \frac{X_{je}^{g-eqH} - X_e^g}{X_{je}^{\mathrm{Hyd}} - X_e^{g-eqH}}. \tag{7c}$$

The actual fraction of gas, F_{je}^{dissol}, added to gas entering element e as the result of hydrate dissolution will be

$$F_{je}^{\mathrm{dissol}} = \min\left[{}^{\mathrm{kinetic}}F_{je}^{\mathrm{dissol}}, {}^{\mathrm{available}}F_{je}^{\mathrm{dissol}}, {}^{\mathrm{thermodyn}}F_{je}^{\mathrm{cryst}}\right]. \tag{7d}$$

Finally, the fractional change in gas flux entering element e that occurs as the result of hydrate crystallization or dissolution within element e is

$$F_e = \sum_{j=1}^{n\mathrm{bins}} F_{je}^{\mathrm{dissol}} - F_e^{\mathrm{cryst}}. \tag{8}$$

[16] The numerical hydrate crystallization/dissolution model proceeds by first solving the temperature equation (1) and then solving for the gas flux, hydrate crystallization, and hydrate dissolution by introducing gas at a rate q_b^g at depth $z = b$. The upward gas flux leaving each element is $1 + F_e$, where F_e is defined by (8). The composition of the gas stream is modified by this hydrate crystallization and dissolution as described by *Cathles and Chen* [2004]. If the gas kinetics are infinitely fast and the dissolution rate is controlled thermodynamically, hydrate in the most unstable bin is dissolved first, followed by less unstable bins until all unstable bins are dissolved or the gas in the element is in thermodynamic equilibrium with any remaining hydrate. The chemical solution is propagated from the deepest to the shallowest element by introducing gas from underlying to overlying elements.

[17] The thermal consequences of hydrate dissolution or crystallization are computed at the end of each time step:

$$S = \frac{\partial q^g}{\partial z} L, \tag{9}$$

where L is the latent heat of hydrate crystallization. This latent heat is used in the next solution of the temperature equation (1) for a second specified Δt. The gas and hydrate composition profiles, and the crystallization and dissolution of hydrate are then calculated again, the heat sources and sinks determined and transmitted to the temperature equation, which is solved for a third specified Δt, etc. The 1 km deep model domain is divided into 60 compacted layers. The layers are specified in terms of their uncompacted thickness and then compacted. The uncompacted layers increase in thickness exponentially for the first 25 layers and are then of constant thickness. The compacted layer thickness thus increases almost exponentially with depth. The first compacted layer in our modeling is 2.1 cm thick, and the last is 22.7 m thick. The solutions reported here use 20 equal-duration time steps. Initial conditions are the steady state, no flow temperature profile. The numerical solution is exactly the same as described by *Cathles and Chen* [2004] except that the latent heat of crystallization is fed back to the temperature equation, and heat advection by gas and water flow is considered. In the previous paper heat sources and advection were assumed negligible, and only conductive temperature changes driven by bottom water temperature variations were considered.

3. Calculation Results

[18] All parameters used in the calculations are listed in Table 1, which also gives values for material properties used and references for the values chosen. Figure 2 shows steady state solutions to the coupled temperature and hydrate crystallization equations. The surface temperature gradient and the depth to the base of the hydrate stability zone depend on the vertical gas mass flux, the percent gas crystallized as hydrate, and the system depth (e.g., depth of the gas source). Lines (solid for 1 km deep gas source and dotted for 2 km deep source) give the analytical solution of equation (3) for 0, 10, and 20% gas crystallized. In solving equation (3) the depth of the hydrate stability zone, z_H, is assumed initially to be its no-flow depth, and z_H is then iteratively adjusted to the converged value using Newton's method. Numerical solutions for the cases of 0 and 10% gas crystallization are shown by data points at mass fluxes of 1.8, 10, 20, 30, 40, and 50 kg m^{-2} yr^{-1} for a gas source at 1 km depth. In the numerical calculations for 10% gas crystallization the kinetic rate constant is adjusted so that the total gas crystallization is ~10%. The solid symbols show the results of numerical simulations where thermal conductivity is uniformly 1 W m^{-1} °C^{-1}. The open symbols show results where thermal conductivity is a function of porosity and temperature (e.g., see later discussion).

[19] Several important things can be seen in Figure 2. First, the close agreement between the analytical and numerical results verifies both. The agreement is nearly exact when $F = 0$ (no hydrate crystallization). When hydrate crystallizes (e.g., $F = 0.1$) the solid symbols of the numeric surface temperature gradient lie slightly above the analytic line. This is because the gas flux in the numeric solution is slower near the surface and the kinetic drive is greater, and thus more hydrate is crystallized there and more latent heat released. The open symbols indicate the minor changes caused by a nonuniform thermal conductivity.

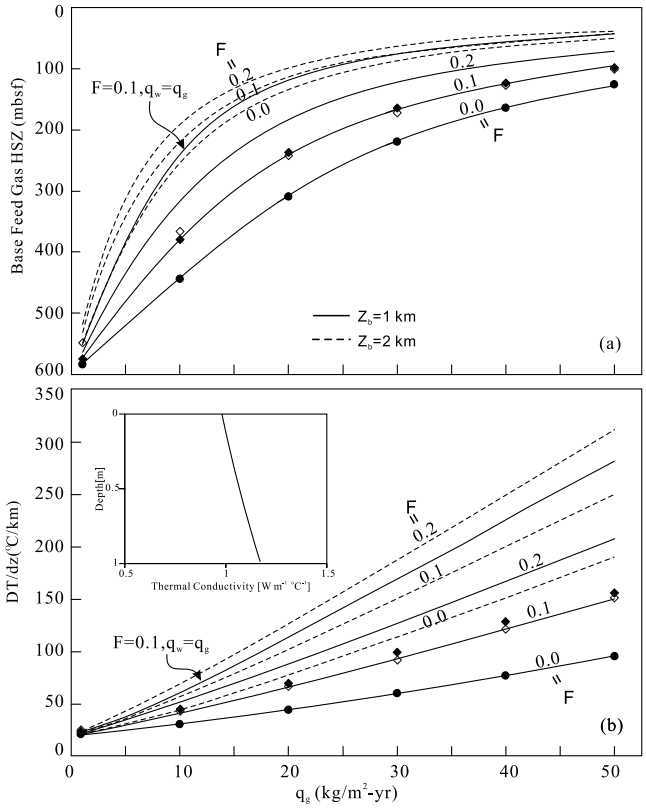

Figure 2. (a) Base of the feed gas hydrate stability zone and (b) surface temperature gradient produced by gas venting and crystallizing a fraction F of its mass as hydrate for times long enough that thermal steady state conditions are attained. Solid lines indicate a system depth of 1 km, and dashed lines indicate a system depth of 2 km. The water flux is zero in all cases except the solid curves identified by arrows and a label that indicates that the water and gas mass fluxes are equal. The lines are calculated from (3), an analytical solution to the steady state heat flow equation for a sediment thermal conductivity of 1 W m^{-1} °C^{-1}. The data points indicate corresponding finite element simulations for this same constant thermal conductivity (solid symbols) and for sediment thermal conductivities that depend on temperature and compacting sediment porosity (open symbols). The variation of sediment thermal conductivity with depth in this latter case is shown in the insert.

[20] Figure 2 shows that heat advection by gas flow alone ($F = 0$ curves) can increase the surface temperature gradient and decrease the depth of the hydrate stability zone dramatically. The importance of heat advection depends strongly on the depth of the gas source. The Peclet number is directly proportional to this depth as indicated in the introduction. At the higher flow rates, the surface temperature gradient for a 2 km deep gas source is nearly twice that

for a gas source at 1 km depth. At gas fluxes of 10 to 20 kg m^{-2} yr^{-1} the base of the hydrate stability zone is hundreds of meters shallower when the gas source is at 2 km (rather than 1 km) depth.

[21] Heat advection is strongly increased if water moves vertically as well as gas. This is indicated in Figures 2a and 2b by one solid curve for 10% hydrate crystallization, a gas source depth of 1 km, and a vertical water mass flux equal to the gas mass flux. For all other curves and data points the water mass flux is zero. These curves show that addition of a water mass flux equal to that of gas affects the surface temperature gradient and the thickness of the hydrate stability zone about as much as increasing the gas source depth from 1 to 2 km.

[22] The latent heat of 10 to 20% hydrate crystallization affects the surface temperature gradient about as much as advection. For example, the increase in dT/dz at $F = 0.1$ is about twice that at $F = 0$ in Figure 2b. The advection of heat and the heat released by hydrate crystallization are also about equal for F between 0.1 and 0.2, as can be seen by substituting parameter values from Table 1 into an equation which equates the heat introduced by gas advection and hydrate crystallization at a gas flow rate q^g:

$$\frac{q^g c_g (T_{z=z_H} - T_S)}{z_H} \sim 0.1 q^g L / z_H.$$

[23] The duration of venting is important. Figure 3 plots the surface temperature gradient against the depth to the base of the hydrate stability zone for different durations of gas venting. The simulations in Figure 3 are designed so that the average fractional venting gas crystallized as hydrate in the subsurface is 0.1 (as at Bush Hill), and some of the pore space is completely filled with hydrate at the end of the simulation (so the vent must shift position). This is done in two steps. First the rate constant, k, is increased by multiplying it by $q_b^g/q_{b,\min}^g$ and all time steps are reduced by dividing them by $q_b^g/q_{b,\min}^g$. Here $q_{b,\min}^g$ is the mass flux of gas into the system when the flux is uniformly distributed over the entire mound (e.g., the "minimal" reference gas flux of 1.8 kg m^{-2} yr^{-1}). The rate constant k was calibrated for this condition by *Chen and Cathles* [2003] and updated by *Cathles and Chen* [2004], and we use this rate constant as a reference value here (see Table 1). If the thickness of the hydrate stability layer did not change with q_b^g, these modifications would assure that the fraction of venting gas crystallized as hydrate is 0.1 as is, on average, the observed case at Bush Hill [see *Chen and Cathles*, 2003, 2004]. Since the HSZ thickness contracts, we need to increase the rate constant by multiplying it by an adjustment factor k_{adj} to assure that, on average over the full simulation, the fraction of feed gas crystallized as hydrate in the subsurface is 0.1. We choose to fix the average value at 0.1 because this gives the greatest likelihood of the model system matching Bush Hill. With k adjusted in this fashion, the duration of each time step is adjusted by multiplying by a t_{adj} such that some of the pores are completely filled with hydrate at the end of the simulation. When this happens, presumably the vent must shift position, so calculating over this time span gives the maximum thermal changes that could occur before the vent shifts location. Results are shown for kinetically and thermodynamically controlled dissolution kinetics. The latter results when the dissolution kinetics are infinitely fast, hence the choice of the label "I" Figure 3 and several of the other diagrams.

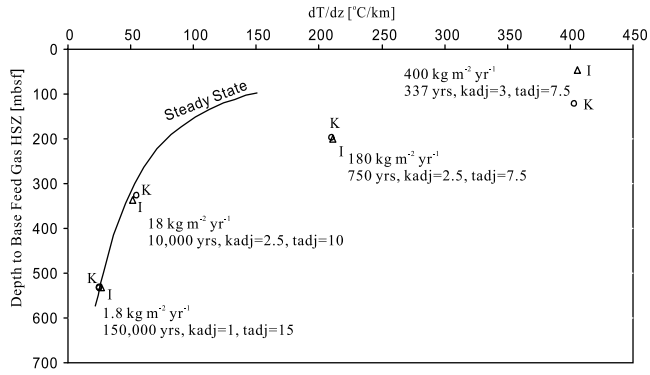

Figure 3. Change in the surface temperature gradient and the depth to the base of the feed gas hydrate stability zone (HSZ) as a function of the gas mass flux. Points indicated the results of finite element simulations that are designed so that on average, over the simulation, 10% of the venting gas crystallizes as hydrate in the subsurface. The duration of the simulation is set so that sediment pores fill completely with hydrate at some depth. Feed rates of 1.8–400 kg m^{-2} yr^{-1} span the range of venting observed at Bush Hill, assuming subsurface gas flow channels are >8 m in diameter. The crystallization rate constant is increased proportionately with feed rate and the duration of venting decreased proportionately. The rate constant and duration are then further adjusted by multiplying by k_{adj} and t_{adj} to compensate for the reduction of thickness of the HSZ, as described in the text. Hydrate dissolution kinetics are kinetically controlled (K) or so rapid (instant kinetics, I) that dissolution is controlled by gas saturation. The solid line labeled "steady state" shows the depth to base of the HSZ and the surface temperature gradient for 10% gas crystallization calculated from equation (3).

[24] Figure 3 shows that at the minimal Bush Hill gas feed rate of 1.8 kg m^{-2} yr^{-1} the pore space will fill with hydrate in 150,000 years, the HSZ thickness is 532 m, and the temperature gradient at the surface is ~26°C/km. These values are very close to the steady state values computed in Figure 2 (e.g., the steady state curve on Figure 3 passes through the 1.8 kg m^{-2} yr^{-1} points). There is little difference between kinetically and thermodynamically controlled dissolution because very little hydrate dissolution occurs. If the gas feed rate is increased to 18 kg m^{-2} yr^{-1}, the thickness of the HSZ is reduced by nearly a factor of 2 and the surface temperature gradient is ~52°C/km. The pores fill with hydrate in 10,000 years. The subsurface temperature is close to its steady state value under this gas feed rate. At a gas feed rate of 180 kg m^{-2} yr^{-1} the pores plug with hydrate in 750 years, but the subsurface temperature is still evolving and is far from the steady state line. At 400 kg m^{-2} yr^{-1} the pores fill with hydrate in ~337 years and the subsurface temperature is even further from steady state. In these cases the surface temperature gradient is hundreds of °C/km and the thickness of the HSZ is <200 m.

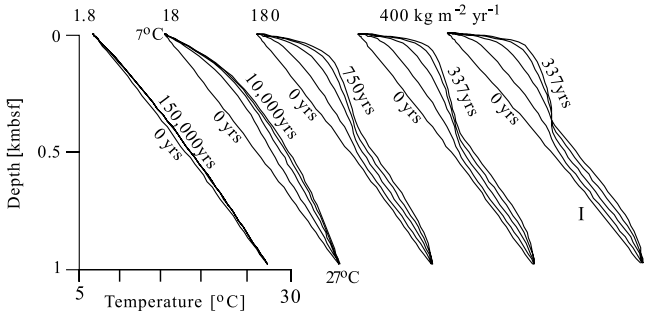

Figure 4. Subsurface temperature profiles for feed gas rates of 1.8–400 kg m^{-2} yr^{-1} for the time durations and parameters indicated in Figure 3 and described in the text. Each set of curves shows the profile at quartiles of the total simulation duration. In each case temperature boundary conditions are 7°C at the surface and 27°C at 1 km depth. The horizontal scale is indicated in the first profile. Subsequent profiles have the same scale but are offset. The dissolution of subsurface hydrate is controlled kinetically for all curves except the last set, labeled I, where the dissolution kinetics are instant.

[25] Figure 4 shows how the subsurface temperature profile evolves in these cases. At the higher gas feed rates, the latent heat of hydrate crystallization produces proportionately larger changes in subsurface temperature. This is because the increasingly limited time interval over which venting fills sediment pores with hydrate minimizes the impact of advective heat transfer, while the release of latent heat remains the same and suffers less conductive heat losses. In this and the following figures we illustrate the difference between very fast (instant = label I) and normal kinetic control of hydrate dissolution for only the fastest venting rate of 400 kg (m^2 yr) $^{-1}$. The difference is noticeable but not important to the conclusions reached.

[26] Figure 5 shows how the base of the feed gas hydrate stability zone moves upward with time for the cases plotted in Figures 3 and 4. The base of the feed gas HSZ is defined in terms of the gas feed composition of $X_b^g = 0.047$. Because the gas wetness (mass fraction C_3 + C_4) decreases as hydrate crystallizes and increases as it dissolves, hydrate may and often does dissolve above or crystallize below the base of the HSZ defined in this fashion. The base of hydrate will not usually coincide with the base of the feed gas HSZ because of the time required to dissolve previously crystallized hydrate.

[27] Figure 6 shows how the pores are filled with hydrate for the cases shown in Figures 3 and 4. By the end of each simulation, hydrate completely fills the pores at some depth. The depth where 100% pore filling occurs is generally close to the surface, and it becomes increasingly close to the surface as the feed rate increases. The depth to the base of the feed gas HSZ (from Figure 5) at the end of each simulation is shown as a dashed line on each diagram. The feed gas HSZ is again the depth at which hydrate would first crystallize from gas of the feed composition, X_b^g = 0.047. From the position of the feed gas HSZ it can be seen that a great deal of the subsurface hydrate is potentially unstable in the high feed rate simulations. By potentially we mean that if surrounded by gas with the feed gas composition it would dissolve. Not all of the potentially unstable hydrate is dissolving in the simulations, however, because the dissolution of deeper hydrate has increased the wetness of the gas stream and the hydrate is stable with respect to this altered gas composition. As noted in the caption of Figure 5, irregularities in some of the curves result from the discritization (binning) of hydrate composition.

[28] Figure 7 shows the how the feed gas composition changes vertically as hydrate is crystallized. At first the shift in composition is extreme, but it flattens as the subsurface warms and previously crystallized hydrate is dissolved. At these later times, the wetness (C_3 + C_4 content) of the gas stream can exceed the wetness of the feed gas due to this dissolution.

[29] Figure 8 shows the fraction of feed gas that is lost to hydrate crystallization (or gained by hydrate dissolution) as a function of time. The curves that compose each case are

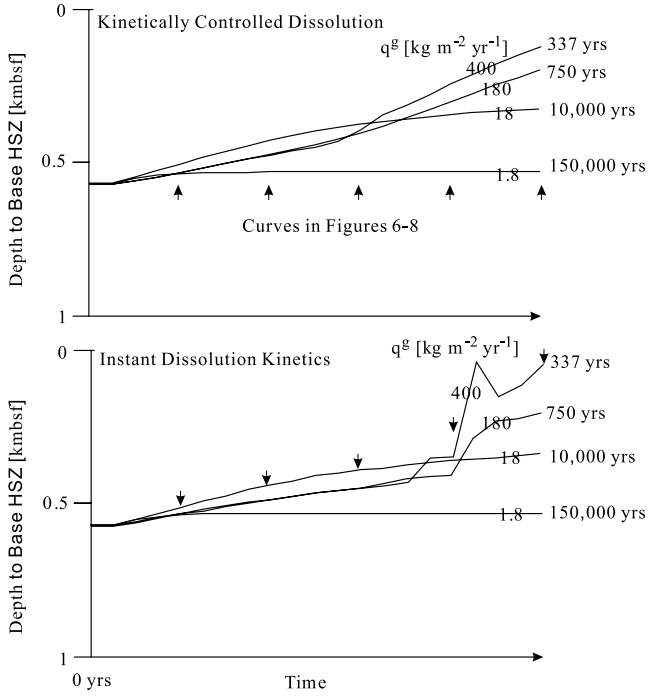

Figure 5. Depth to the base of the hydrate stability zone for gas of feed composition (mass fraction C_3 + C_4 = 0.047) for feed rates from 1.8 to 400 kg m^{-2} yr^{-1}. Arrows indicate the quintiles of the simulation interval that are plotted in Figures 6–8. Subsurface temperatures (and the depth to the base of the feed gas HSZ) are influenced by the limited duration venting can occur before the vent is plugged with hydrate. (a) Depth to the base of the feed gas HSZ if dissolution is kinetically controlled. (b) Depth to the base of the feed gas HSZ if hydrate dissolution is infinitely fast and controlled thermodynamically by changes in gas composition. The jaggedness of the instant dissolution curves for the faster venting rate cases results from binning hydrate in discrete composition bins. Discontinuities in heat generation result when bins become depleted of hydrate. Curves end when the vent is plugged at some depth with hydrate. The time required for this to occur is indicated at the left end of each curve. The base of the feed gas HSZ at the end of each simulation is plotted as dashed lines in Figures 6–8.

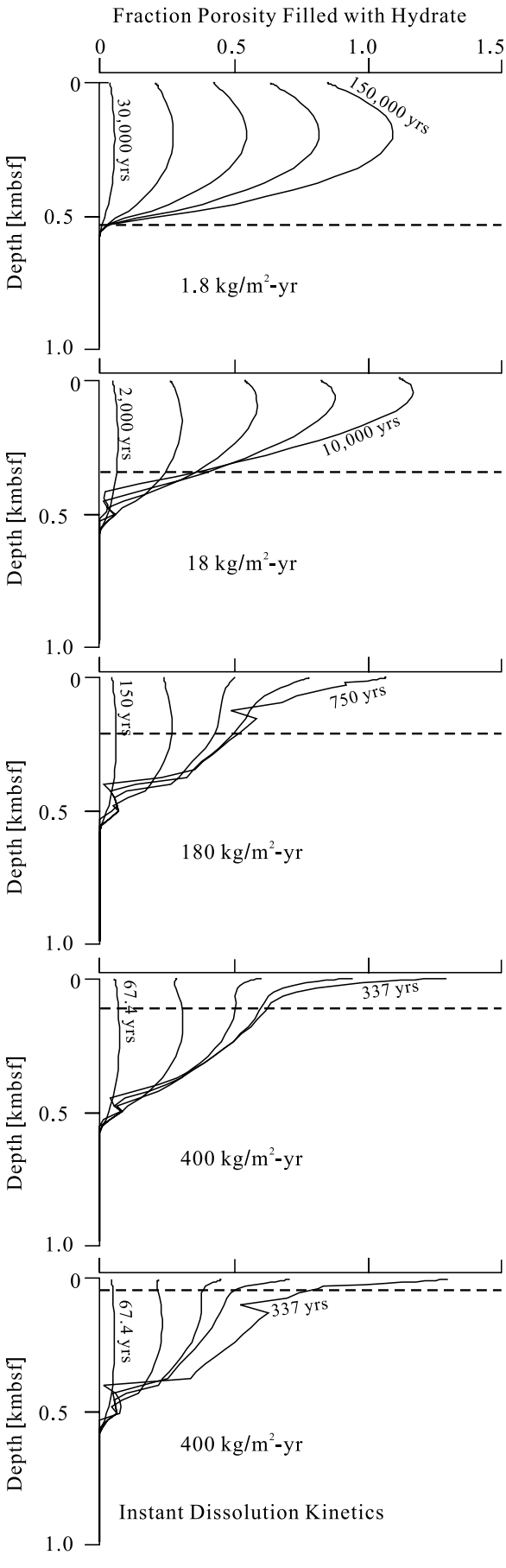

Figure 6. Fraction of the pore space filled with hydrate as a function of depth for the simulations shown in Figure 3. Curves in each set are at quintiles of the simulation time as shown by arrows in Figure 5. Simulation duration is adjusted so that the fraction of hydrate fill is 1 at the end of the simulation. The dashed line indicates the depth to the base of the hydrate stability zone (HSZ) for gas of feed composition. This figure shows that previously crystallized hydrate is slow to dissolve and a good deal of hydrate persists below the base of the feed gas HSZ. This is allowed because the hydrocarbon content of the gas is increased by hydrate dissolution and this slows the rate of hydrate dissolution.

quintiles of the simulation time, and it can be seen in all cases that the mean (over time) gas loss at the surface is close to ~10%, which was our design criteria. This mean loss is indicated by arrows at the top of each diagram. Again it can be seen that at depth the gas flux is increased slightly over the initial feed rate (negative fraction crystallized) due to hydrate dissolution.

[30] Finally, Figure 9 shows the composition of hydrate accumulated for the 180 kg m^{-2} yr^{-1} cases shown in the previous figures. The hydrate deposition steps to the right in bands which correspond to the time steps of the simulation. With this in mind it can be seen that the mass fraction C_3 + C_4 in crystallized hydrate increases with time, and most strongly so very near the surface. The composition of the hydrate bins is given in Table 2. The shape of the final (750 yr) curves are the same as in the final 180 kg m^{-2} yr^{-1} curves in Figure 6, except here we plot the mass of gas per unit volume accumulated as hydrate rather than the fraction of the sediment pores filled with hydrate.

4. Discussion

[31] We verified our calculations in two ways. First the good agreement between the analytical steady state and numerical calculations at slow flow rates verifies both. Second by increasing the number of elements from 60 to 100 while keeping the surface element thickness ~2.2 cm so that the thickness of the deepest element decreased from 22.7 to 14.4 m, we found the depth of the feed gas HSZ changed by <0.1m. The calculations are adequately converged for the conclusions we draw in this paper.

[32] The most important result is documentation of the dramatic decrease in thickness of the feed gas hydrate stability zone and increase in the surface temperature gradient that occurs for gas venting rates in the range inferred to be occurring at seafloor gas vents such as exist at Bush Hill. If these gas discharges occurred over broad enough areas for the one-dimensional calculations to be valid, heat advection and latent heat released from hydrate crystallization decreases the thickness of the feed gas HSZ from 590 m to less than 100 m, and increase the surface temperature gradient from 20 to >400°C/km. For a gas flow of 1.8 kg m^{-2} yr^{-1} and the thermal conductivity profile shown in Figure 2, the depth to the base of the HSZ is 570 m and the surface temperature gradient 21°C/km. Thus even at a gas flux of 1.8 kg m^{-2} yr^{-1} (our reference minimal discharge for the Bush Hill mound) will perturb the sub-

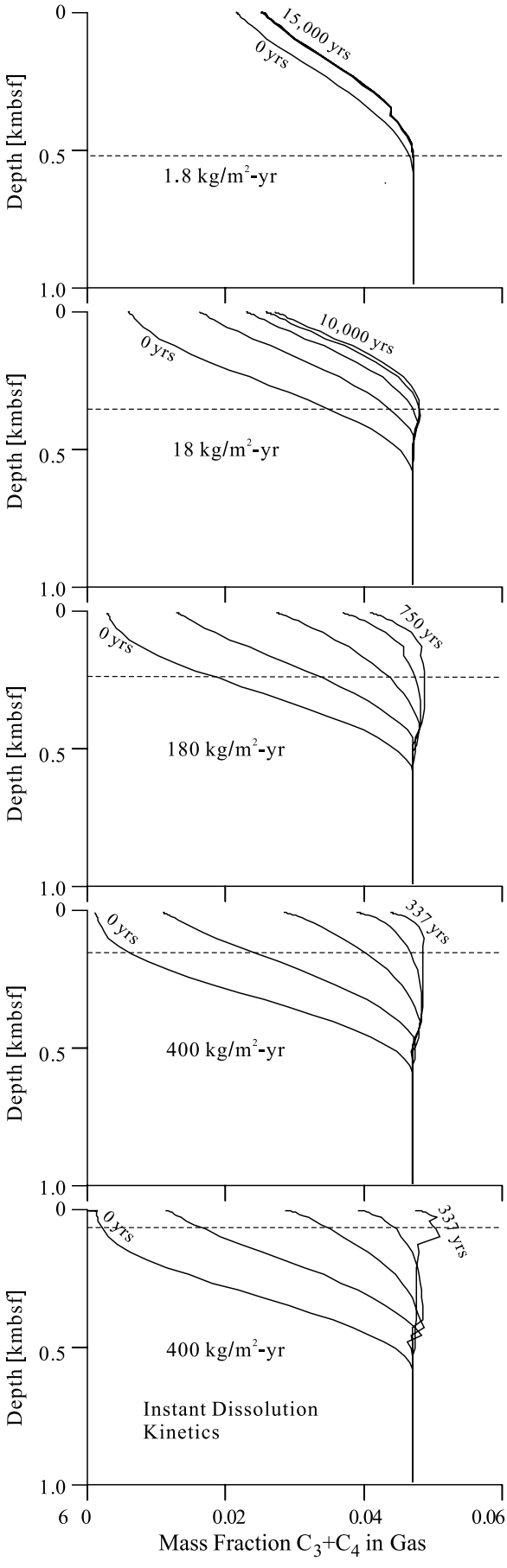

surface temperature profile if the gas discharge is aerially extensive. At the faster gas venting rates the subsurface temperature changes become extreme. The calculations show some interesting features. The depth at which gas is fed laterally to the vent plumbing system is an important control on the potential thermal impact of venting. As venting rates increase, dynamic processes associated with the venting become potentially more important. For example, our calculations indicate that at high gas venting rates hydrate will be increasingly concentrated at or very near the surface where it is susceptible to dissolution. The near-surface hydrate will rich in $C_3 + C_4$ (Figure 9).

[33] Our calculations are weakly specialized to Bush Hill because we adjust our model hydrate crystallization kinetics so the time averaged fraction of the feed gas crystallized as hydrate is 0.1. Assuming water does not move with the gas, the thermal perturbations and chemical changes we report in Figures 3–9 are the maximum changes that could reasonably occur at a seafloor gas vent such as Bush Hill. The thermal perturbations calculated are maximum for two reasons: First, we limit the time duration of venting to that at which the sediment pores will fill with hydrate at some depth (usually very near the surface). When this occurs, venting will presumably shift to another location. In fact, the shift will likely occur before the pores are fully plugged because sediment permeability will be greatly reduced before the pores are fully plugged. The thermal impact of gradual flow reduction will depend on how weaker heat advection trades off against a longer heat advection. We do not explore this trade-off in this paper. The gas flux in our models is constant until the pores are fully plugged with hydrate at some depth and the simulation is terminated. The perturbation in subsurface temperature could be much more severe if the time duration of venting was not limited by hydrate plugging (as illustrated by the difference between the solid curve and points in Figure 3). Second, our calculations are one-dimensional and assume no heat is lost horizontally. This is a major restriction on the application of the calculations presented here because it requires that the lateral dimensions be similar to the vertical interval of gas venting. Gas vents as broad as 500 m diameter (a typical thickness of the hydrate stability zone) seem to occur, but the distributed (over time and space) rate of gas venting across such areas is almost certainly not as high as the

Figure 7. Mass fraction $C_3 + C_4$ in gas moving to the seafloor from 1 km depth at various rates and for the simulation conditions indicated in Figure 3. Curves in each set are at quintiles of the simulation time as shown by arrows in Figure 5. The kinetic rate constant controlling hydrate crystallization is adjusted in each case so that the average (over the simulation) fraction of gas lost to hydrate crystallization is 0.1, the mean observed crystallization inferred from vent chemistry at Bush Hill. The dashed line indicates the depth to the base of the hydrate stability zone (HSZ) for gas of feed composition. This figure shows how subsurface warming and hydrate dissolution flattens the gas composition-depth profile with time. The gas wetness ($C_3 + C_4$ content) can exceed that of the feed gas due to dissolution of underlying hydrate. The jaggedness in some curves results from depletion of hydrate bins.

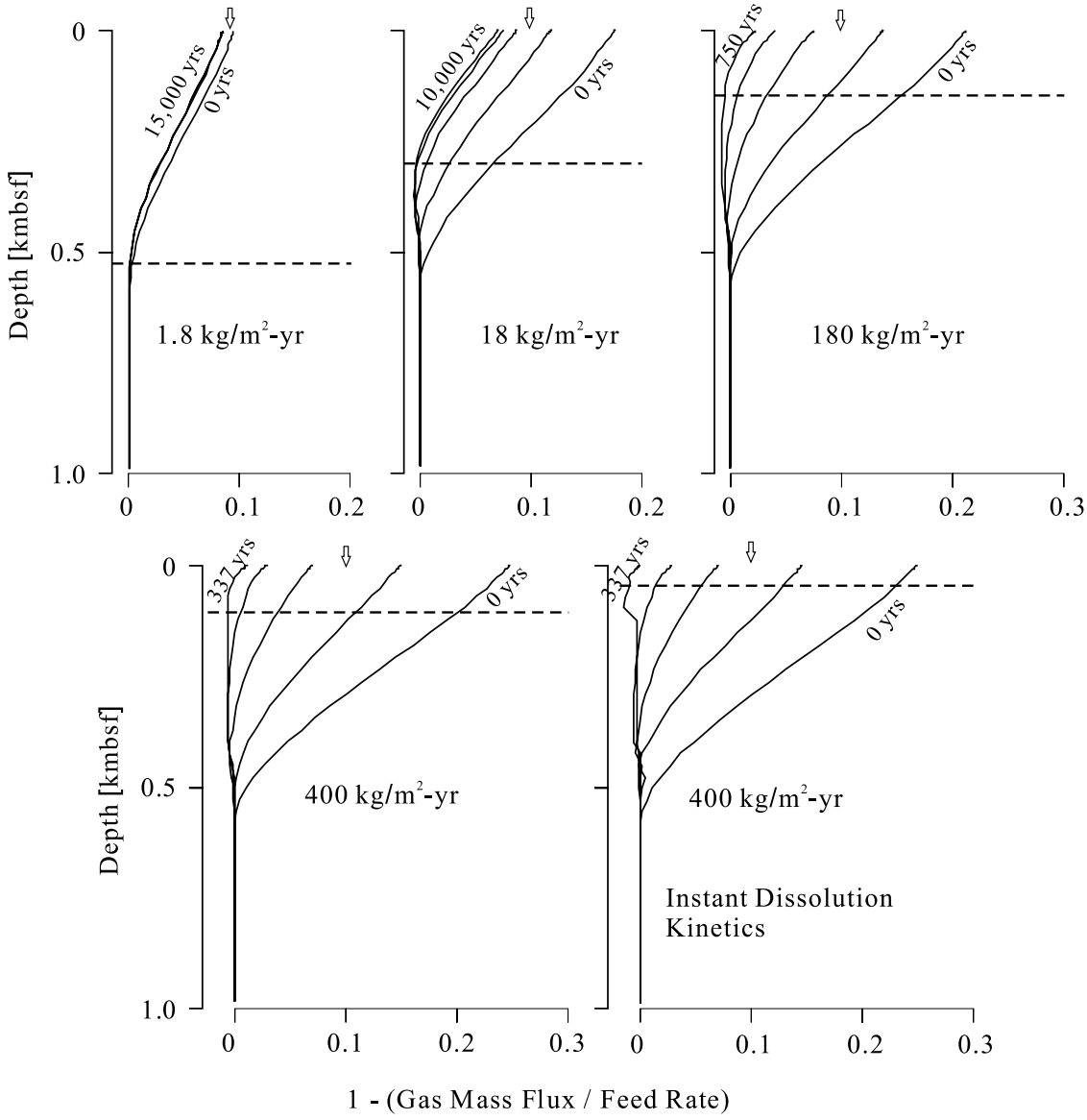

Figure 8. Fractional change in the feed rate caused by hydrate crystallization and dissolution for different feed rates and simulation specification indicated in Figure 3. Curves in each set are at quintiles of the simulation time, as shown by arrows in Figure 5. Dashed line indicates the depth to the base of the hydrate stability zone (HSZ) for gas of feed composition. The time-averaged loss of gas to hydrate is indicated by small arrows at the top of each set of curves. It is close to our design criterion of 0.1 in all cases. Gas loss to hydrate is rapid when a vent initiates (0 year), and drops and even become negative (indicating gas is gained by hydrate dissolution) as the vent plugs with hydrate.

maximum rates presented here. High gas discharge over broad areas could occur if a gas reservoir ruptured, however. This paper calculates how aerially extensive weak to rapid gas venting and hydrate crystallization perturbs subsurface temperatures.

[34] Of course the thermal perturbations are not maximum if water vents along with the gas. It is shown in Figure 2 for example, that if water vents at the same rate as gas, the subsurface temperature change is dramatically increased. The consequences of water entrainment may be reduced if pore water convection is induced by the temperature perturbations caused by the gas and water venting.

[35] Water flow may be important for another reason. The hydrate structure incorporates water and gas but not salt. Thus hydrate crystallization will increase the salinity of the pore waters from which it crystallizes. Pore water salinity affects the equilibrium between gas and hydrate [e.g., *Davie et al.*, 2004; *Milkov et al.*, 2004; *Torres et al.*, 2004]. The empirically calibrated kinetic models that we use here do not account for the salinity changes that attend hydrate crystallization. In effect we incorporate the impact of these changes in our empirical calibration. Future models should include salt generation and advection.

[36] Are there any seafloor observations that suggest thermal perturbations at the high end of what our calculations show can be expected? Surface heat flows in areas where bottom water temperatures vary is complicated because the bottom water temperature variations produce

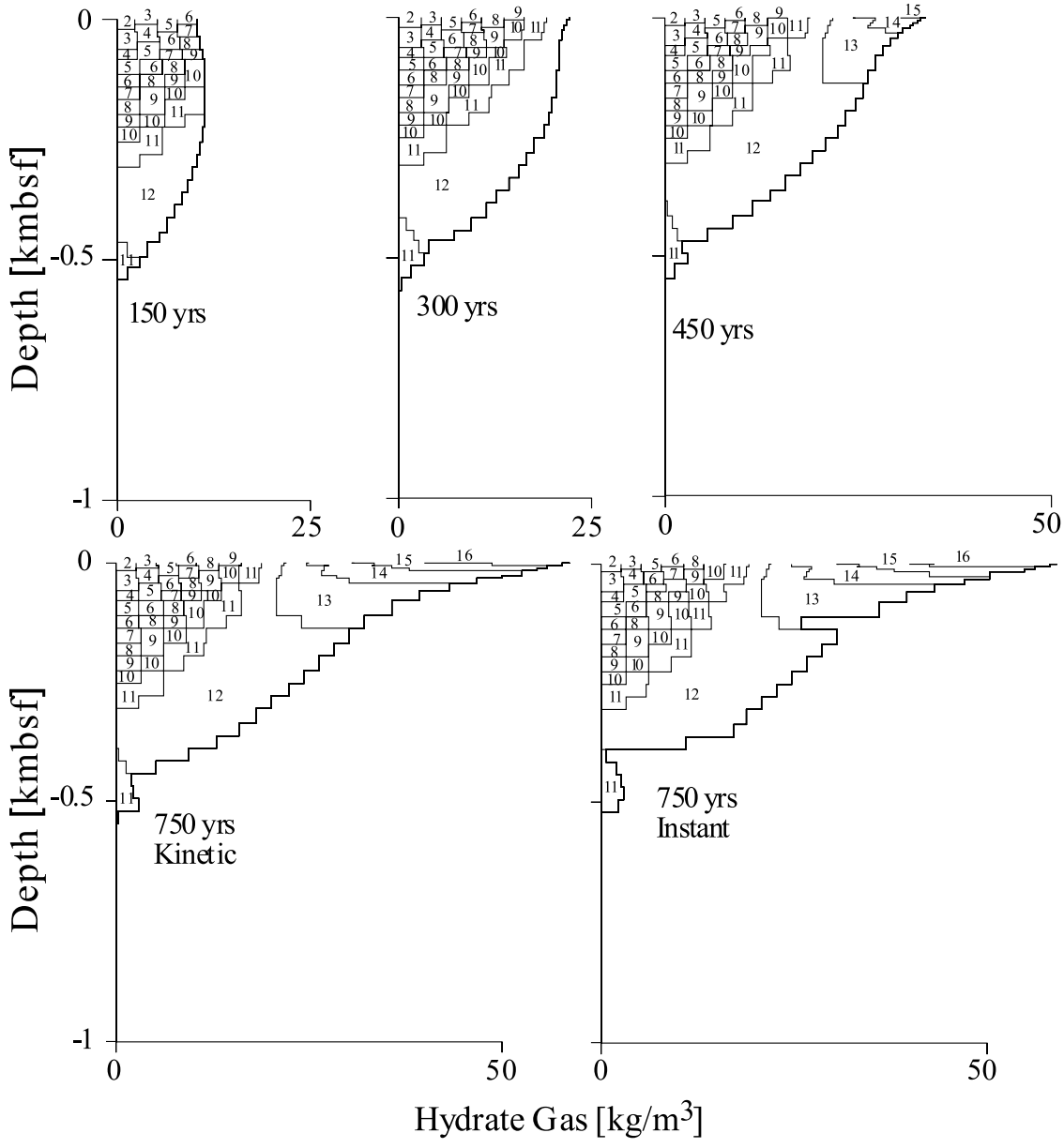

Figure 9. Profiles of subsurface hydrate accumulation showing hydrate composition for the 180 kg m^{-2} yr^{-1} case. The last pair of plots compares the final results for kinetic and instant dissolution kinetics. The other plots show the accumulation of hydrate with time under kinetic dissolution control. Vertical bands in each plot show the deposition of hydrate over time in the subsurface depth intervals spanned by the computational finite elements. Hydrate composition is indicated by bin numbers (see Table 2). Hydrate dissolution at depth and crystallization of hydrate rich in $C_3 + C_4$ hydrocarbons increasingly close to the surface as time progresses are notable features of the figure.

thermal waves in the shallow subsurface and temperature gradients at the surface produced in this fashion can be high and either positive (temperature increasing with depth) or negative [*Cathles and Nunns*, 1991]. We are aware that temperature gradients of hundreds of mK m^{-1} have been measured near the Bush Hill mound (J. Brooks, TDI-Brooks, personal communication, 2005), but negative gradients of nearly this magnitude are recorded in the same data set, which suggests a correction for bottom water temperature variation is required. Temperature gradient profiles that appear not to be affected by bottom water temperature variations have been measured across mud diapers in the offshore Louisiana Gulf of Mexico [*Ruppel et al.*, 2005]. These profiles show that temperature gradients increase from 40 mK m^{-1} near a mud mound in Garden Banks to 425–557 mK m^{-1} at its crest, and from 24.5 to 435 mK m^{-1} over a mud mound in Mississippi Canyon Block 852. Concave downward salinity profiles suggest mud fluxes of 0.1 and 0.15 m yr^{-1}, respectively. Although gas may also move through the mud, the heat advection is dominated by the mud diapirism, and so these measurements do not confirm that gas fluxes alone could produce

400 mK m^{-1} temperature gradients at the surface. *Ruppel et al.* [2005] emphasize that advection of heat by mud diapirism may greatly reduce the hydrate inventory in an area. Advection of heat by gas venting in broad areas at modest rates could significantly reduce the thickness of the feed gas hydrate stability zone, but reduction of the hydrate resource in this case is limited by the fact that the dissolution of previously crystallized hydrate is slow and the potential dissolution is incomplete when the vent plugs with hydrate and gas flow ceases (Figure 6).

5. Conclusions

[37] In this paper we present a new analytical solution of the one-dimensional steady state advective heat flow equation that includes the latent heat of hydrate crystallization. We also present transient finite element 1-D solutions of the transient advective temperature equation that includes the latent heat of hydrate crystallization. The duration of the transient solutions is limited to that at which pores plug with hydrate at some depth, and the kinetics of hydrate crystallization is adjusted so the time average fraction of feed gas crystallizing as hydrate is 0.1. The numerical simulations show that gas venting at rates similar to those observed could reduce the depth to the base of the feed gas hydrate stability zone and increase the surface temperature gradient substantially if the diameter of the area of gas venting is comparable to the interval of vertical gas flow. Warming of the vent decreases the vertical extent of the feed gas hydrate stability zone, redistributes hydrate to shallower depths, and alters hydrate chemistry. Our calculations assume no lateral loss of heat and thus provide an upper bound on temperature and chemical changes gas venting could produce. Lateral losses of heat, salinity changes associated with hydrate crystallization and dissolution, and pore water advection accompanying the gas stream or driven by the temperature anomalies produced by gas venting will need to be considered in later papers.

[38] **Acknowledgments.** We are grateful to H. Roberts, an Associate Editor of JGR, and two anonymous reviewers for comment that greatly improved the manuscript. Comments on an earlier manuscript by Wenye Xu further stimulated our interest the subsurface temperature perturbations that might be produced by gas venting. Chen acknowledges the support of the Chinese Academy of Sciences (projects KZCX3-SW-224, KZCX2-SW-309, and KZCX3-SW-219). Funds from the corporate sponsors of the Global Basins Research Network have supported Chen on five visits to the United States.

References

Bredehoeft, J. D., and I. S. Popadopulos (1965), Rates of vertical ground water movement estimated from the earth's thermal profile, *Water Resour. Res.*, *1*, 325–328.

Cathles, L. M., and D. F. Chen (2004), A compositional kinetic model of hydrate crystallization and dissolution, *J. Geophys. Res.*, *109*, B08102, doi:10.1029/2003JB002910.

Cathles, L. M., and S. Losh (2004), Hydrocarbon generation, migration, and venting in a portion of the offshore Louisiana Gulf of Mexico, *Leading Edge*, *23*, 760–765.

Cathles, L. M., and A. G. Nunns (1991), A temperature probe survey on the Louisiana shelf: Effects of bottom-water temperature variations, *AAPG Bull.*, *75*, 180–186.

Chen, D. F., and L. M. Cathles (2003), A kinetic model for the pattern and amounts of hydrate precipitated from a gas steam: Application to the Bush Hill vent site, Green Canyon Block 185, Gulf of Mexico, *J. Geophys. Res.*, *108*(B1), 2058, doi:10.1029/2001JB001597.

Chen, D. F., L. M. Cathles, and H. H. Roberts (2004), The chemical signatures of variable gas venting at hydrate sites, *Mar. Pet. Geol.*, *21*, 317–326.

Cook, D., and P. D'Onfro (1991), Jolliet Field thrust structure and stratigraphy, Green Canyon Block 184, offshore Louisiana, *Trans. Gulf Coast Assoc. Geol. Soc.*, *41*, 100–121.

Davie, M. K., O. Y. Zatsepina, and B. A. Buffett (2004), Methane solubility in marine hydrate environments, *Mar. Geol.*, *203*, 177–184.

De Beukelaer, S. M., I. R. MacDonald, N. L. Guinnasso, and J. A. Murray (2003), Distinct side-scan sonar, RADARSAT SAR, and acoustic profiler signatures of gas and oil seeps on the Gulf of Mexico slope, *Geo Mar. Lett.*, *23*, 177–186.

Dickens, G. R., and M. S. Quinby-Hunt (1997), Methane hydrate stability in pore water: A simple theoretical approach for geophysical applications, *J. Geophys. Res.*, *102*, 773–783.

Hochstadt, H. (1964), *Differential Equations*, 294 pp., Dover, Mineola, N. Y.

Hyndman, R. D., and E. E. Davis (1992), A mechanism for the formation of methane hydrate and seafloor bottom simulating reflectors by vertical fluid expulsion, *J. Geophys. Res.*, *97*, 7025–7041.

Kvenvolden, K. A., and T. D. Lorenson (2001), The global occurrence of natural gas hydrates, in *Natural Gas Hydrates: Occurrence, Distribution, and Detection*, *Geophys. Monogr. Ser.*, vol. 124, edited by C. K. Paull and W. P. Dillon, pp. 3–18, AGU, Washington, D. C.

Leifer, I., and I. R. MacDonald (2003), Dynamics of the gas flux from shallow gas hydrate deposits: Interaction between oily hydrate bubbles and the oceanic environment, *Earth. Planet. Sci. Lett.*, *21*, 411–424.

Luo, M., J. R. Wood, and L. M. Cathles (1994), Prediction of thermal conductivity in reservoir rocks using fabric theory, *J. Appl. Geophys.*, *32*(4), 321–334.

MacDonald, I. R., W. W. Sager, and M. B. Peccini (2003), Association of gas hydrate and chemosynthetic fauna in mounded bathymetry at mid-slope hydrocarbon seeps: Northern Gulf of Mexico, *Mar. Geol.*, *198*, 133–158.

Milkov, A. V., and R. Sassen (2003), Preliminary assessment of resources and economic potential of individual gas hydrate accumulations in the Gulf of Mexico continental slope, *Mar. Pet. Geol.*, *20*, 111–128.

Milkov, A. V., G. R. Dickens, G. E. Claypool, Y.-J. Lee, W. S. Borowski, M. E. Torres, W. Xu, H. Tomaru, A. M. Trehu, and P. Schultheiss (2004), Co-existence of gas hydrate, free gas, and brine within the regional gas hydrate zone at Hydrate Ridge (Oregon margin): Evidence from prolonged degassing of a pressurized core, *Earth Planet. Sci. Lett.*, *222*, 829–843.

Rempel, A. W., and B. A. Buffett (1997), Formation and accumulation of gas hydrate in porous media, *J. Geophys. Res.*, *102*, 10,151–10,164.

Revil, A., and L. M. Cathles (2002), Fluid transport by solitary waves along growing faults: A field example from the South Eugene Island Basin, Gulf of Mexico, *Earth Planet. Sci. Lett.*, *202*, 321–335.

Roberts, H. H., and R. S. Carney (1997), Evidence of episodic fluid, gas, and sediment venting on the northern Gulf of Mexico continental slope, *Econ. Geol.*, *92*, 863–879.

Rueff, R. M., E. D. Sloan, and V. F. Yesavage (1988), Heat capacity and heat of dissociation of methane hydrates, *Am. Inst. Chem. Eng.*, *34*, 1468–1476.

Ruppel, C., G. R. Dickens, D. G. Castellini, W. Gilhooly, and D. Lizarralde (2005), Heat and salt inhibition of gas hydrate formation in the northern Gulf of Mexico, *Geophys. Res. Lett.*, *32*, L04605, doi:10.1029/2004GL021909.

Sloan, E. D. (1998), *Clathrate Hydrates of Natural Gases*, 2nd ed., 628 pp., CRC Press, Boca Raton, Fla.

Torres, M. E., K. Wallmann, A. M. Trehu, G. Bohrmann, W. S. Borowski, and H. Tomaru (2004), Gas hydrate growth, methane transport, and chloride enrichment at the southern summit of Hydrate Ridge, Cascadia margin off Oregon, *Earth Planet. Sci. Lett.*, *226*, 225–241.

Turcotte, D. L., and G. Schubert (2002), *Geodynamics*, 456 pp, Cambridge Univ. Press, New York.

Xu, W., and C. Ruppel (1999), Predicting the occurrence, distribution, and evolution of methane gas hydrate in porous marine sediments, *J. Geophys. Res.*, *104*, 5081–5096.

L. M. Cathles, Department of Earth and Atmospheric Sciences, Cornell University, Ithaca, NY 14853-1504, USA. (cathles@geology.cornell.edu)

D. F. Chen, Key Laboratory of Marginal Sea Geology of Guangzhou Institute of Geochemistry, Chinese Academy of Sciences, Wushan, Guangzhou, Guangdong 510640, China.